

New Models and Super-Resolution Techniques for Short-Range Radar: Theory and Experiments

B. Mamandipoor⁽¹⁾, A. Arbabian⁽²⁾ and U. Madhow⁽¹⁾

(1) ECE Department, University of California, Santa Barbara, CA, USA

(2) EE Department, Stanford University, Stanford, CA, USA

Emails: {bmamandi, madhow}@ece.ucsb.edu, arbabian@stanford.edu

Abstract—Short-range millimeter (mm) wave radar imaging has significant potential for emerging applications such as handheld-based gesture recognition and vehicular situational awareness. In this paper, we develop a theoretical framework for an array of monostatic elements for this purpose. We show that we must account for form factor and complexity constraints in a manner that is quite different from that of conventional radar, and introduce new models and algorithms validated by experimental results. Our main results include (a) identification of the number of degrees of freedom as a function of scene and array geometry, (b) demonstrating that grating lobes seen for the conventional point scatterer model when we employ sparse arrays can be eliminated by using spatial aggregation, using patch-based scatterer models as our dictionary, (c) optimization of patch size based on estimation-theoretic bounds, (d) super-resolution using a recently developed algorithm combining Newton methods with greedy pursuit.

I. INTRODUCTION

While the long-range radar systems used in avionics and defense systems today are bulky and expensive, recent advances in silicon offer the possibility of low-cost, highly integrated radar systems at mm wave and beyond [1]. The latter are particularly well matched to emerging short-range active radar imaging applications such as autonomous vehicle navigation, and human gesture recognition on a handheld device. In this paper, we consider real-time imaging using an array of transceiver elements. In order to minimize cost and complexity, we wish to use as few elements as possible, while enforcing minimal or no cooperation between the array elements during data acquisition. Specifically, we consider a “sparse monostatic” array architecture in which there is no synchronization between the transceiver elements that are spatially separate. The constraints on spatial extent for the array and the scene, together with the sparsity of array, implies that the standard framework for long-range radar does not apply, and motivates the effort in this paper to develop new models and algorithms.

Contributions: Our contributions are summarized as follows. We first show that constraints on array form factor and scene extent limit the number of degrees of freedom. Employing more array elements than the number of degrees of freedom can improve signal-to-noise ratio (SNR), but does not improve normalized measures of target discrimination. Second, we explore the effect of sparse arrays with number of elements significantly smaller than the degrees of freedom. For the

conventional point scatterer primitive, it is well known that sparse arrays create grating lobes (i.e., targets in spatially separated locations can have highly correlated responses), thereby creating fundamental ambiguities. At short ranges, however, targets contain extended features (consisting of a continuum of points), and are not well-modeled by a small number of point scatterers. We introduce the concept of “spatial aggregation,” which provides the flexibility of constructing a dictionary in which each atom corresponds to a collection of point scatterers. Specifically, we show that a patch-based primitive alleviates the problem of grating lobes with sparse arrays, and show how to choose the patch size based on estimation-theoretic bounds: elimination of grating lobes is related to the SNR threshold at which the Ziv-Zakai bound (ZZB) converges to the Cramér-Rao bound (CRB). Third, we show that, while spatial aggregation helps with standard “matched filter” style imaging, it also provides an effective basis for sparse reconstruction techniques. We illustrate the efficacy of our ideas and algorithms using a testbed in which a monostatic transceiver at 60 GHz (wavelength of $\lambda = 0.5$ cm) is used to emulate (for static scenes) a two-dimensional (2D) array using a movable platform.

Related work: The deterioration of imaging performance due to grating lobes caused by undersampling is well known [2], [3]. Prior approaches for grating lobe suppressing include the use of shaped waveforms and aperture diversity [2], employing a multistatic array (synchronization) [4], frequency diversity (wideband) [5], and incorporating Doppler information from moving targets [6]. However, to our knowledge, there is little prior work done on improving scene *modeling* to combat grating lobes. Our spatial aggregation approach, however, may be viewed as falling within the general framework of synthesis-based sparse signal representation, which has been an active area of research for the past decade or so [7], [8]. One of the main advantages of this approach is that it explicitly incorporates the prior information regarding the nature of the aperture (e.g., sparsity level and the geometry of the array), and the nature of the scene (e.g., shape/size/type of targets in the scene) in constructing the dictionary and forming the image. An implicit assumption behind our patch-based primitive is that the scene reflectivity is *lowpass* (i.e, it varies slowly in space). Finally, the sparse reconstruction framework is based on a variant of the Newtonized Orthogonal

Matching Pursuit algorithm developed in [9], [10]. While this algorithm was shown to represent the state of the art in terms of empirical performance for a classical frequency estimation problem, more detailed comparison with competing algorithms for alternative models such as the one in this paper remains an open issue beyond our current scope.

II. DEGREES OF FREEDOM AND GRATING LOBES

Consider the 1-dimensional array geometry depicted in Figure 1 (generalization to two dimensions is straightforward). Let L_1 , L_2 , and D denote the size of the aperture, the size of the scene, and the distance between the aperture and the scene, respectively. We consider the nominal values $L_1 = L_2 = 15$ cm and $D = 30$ cm in our simulations. The inter-element spacing of a uniform linear array comprised of N elements is given by $d = L_1/(N-1)$. Let Ψ be a set that contains the locations of all the point scatterers in the scene, and $\Gamma(x') : \Psi \rightarrow \mathbb{C}$ denote the complex reflection coefficient corresponding to the point scatterer at location x' . The scene response is an N -dimensional vector denoted by $\mathbf{r} \in \mathbb{C}^N$, for which the n^{th} element corresponds to the monostatic transceiver located at x_n , and is given by

$$r[n] = \int_{x' \in \Psi} \Gamma(x') e^{-j2kR(x', x_n)} dx', \quad (1)$$

where $k = 2\pi/\lambda$ is the wavenumber, and $R(x', x_n) = \sqrt{D^2 + (x' - x_n)^2}$ is the path length from the transceiver location to the point scatterer at location x' . We use a first order Taylor approximation to compute the path length, $R(x', x_n) \approx D + \frac{(x' - x_n)^2}{2D}$. Therefore,

$$r[n] \approx e^{-j2kD} \int_{x' \in \Psi} \Gamma(x') e^{-j\frac{k}{D}(x' - x_n)^2} dx'. \quad (2)$$

Grating lobes appear when two spatially separated point

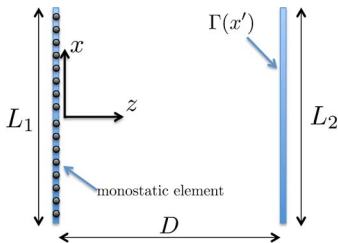


Fig. 1. Geometry of 1-dimensional monostatic imaging

scatterers in the scene generate highly correlated responses. Let us consider two point scatterers located at x'_1 and x'_2 (i.e., $\Psi_i = \{x'_i\}$ for $i \in \{1, 2\}$), with responses denoted by \mathbf{r}_1 and

\mathbf{r}_2 , respectively. The correlation between the two responses is given by

$$\begin{aligned} \mathbf{r}_1^H \mathbf{r}_2 &\approx \sum_{n=1}^N \Gamma_1^* \Gamma_2 e^{j\frac{k}{D}(x'_1 - x_n)^2} e^{-j\frac{k}{D}(x'_2 - x_n)^2} \\ &= \Gamma_1^* \Gamma_2 e^{j\frac{k}{D}(x'_1{}^2 - x'_2{}^2)} \sum_{n=1}^N e^{j\frac{2k}{D}(x'_2 - x'_1)x_n} \\ &= c_1 \frac{\sin(N\rho/2)}{\sin(\rho/2)} = c_1 \text{Dir}(\rho), \end{aligned} \quad (3)$$

where c_1 is a complex coefficient with $|c_1| = |\Gamma_1||\Gamma_2|$, and $\text{Dir}(\rho) = \frac{\sin(N\rho/2)}{\sin(\rho/2)}$ is the well-known Dirichlet kernel with $\rho \triangleq \frac{2k}{D}(x'_2 - x'_1)d$. Note that $\rho \in [0, 2kdL_2/D]$; that is, it takes values in an interval that depends on the signal wavelength and the geometry of the imaging problem. Additionally, $\|\mathbf{r}_i\| = |\Gamma_i|\sqrt{N}$ for $i \in \{1, 2\}$, so that the normalized correlation function is given by

$$\frac{|\mathbf{r}_1^H \mathbf{r}_2|}{\|\mathbf{r}_1\| \|\mathbf{r}_2\|} = \frac{1}{N} \text{Dir}(\rho). \quad (4)$$

The Dirichlet kernel is a periodic function with period 2π , hence the condition for avoiding aliasing, or grating lobes, translates to constraining the visible range of ρ to be less than 2π , or $\frac{2kdL_2}{D} \leq 2\pi$. This yields $\frac{2L_1L_2}{D\lambda} + 1 \leq N$. For our nominal parameter values, we obtain that $N \geq 31$.

Figure 2 shows the magnitude of the normalized correlations (also known as the ambiguity function) for point scatterers $x'_1 = 4\text{cm}$ fixed, and x'_2 varying in the interval $[-7.5, 7.5]\text{cm}$, for $N = 15$ and $N = 31$. We see that setting $N = 15$ leads to a grating lobe artifact at $x_{\text{gl}} \approx -3.5\text{cm}$. The separation between the true point location and the grating lobe is calculated by setting $\rho = 2m\pi$, for $m \in \mathbb{Z}$. It is easy to see that the first grating lobe is at distance $\Delta x = |x_{\text{gl}} - x'_1| \approx \frac{\lambda D}{2d}$ from the true point location (e.g. $\Delta x \approx 7.5\text{cm}$ for $N = 15$).

Another important observation is that increasing the number of array elements beyond $\frac{2L_1L_2}{\lambda D} + 1$ has little impact on the normalized correlation function. This is because, for $N \gg \frac{2L_1L_2}{\lambda D}$, we have

$$\begin{aligned} \frac{|\mathbf{r}_1^H \mathbf{r}_2|}{\|\mathbf{r}_1\| \|\mathbf{r}_2\|} &= \frac{1}{N} \frac{\sin\left(\frac{kL_1N}{D(N-1)}(x'_2 - x'_1)\right)}{\sin\left(\frac{kL_1}{D(N-1)}(x'_2 - x'_1)\right)} \\ &\approx \frac{1}{N} \frac{\sin\left(\frac{kL_1}{D}(x'_2 - x'_1)\right)}{\frac{kL_1}{D(N-1)}(x'_2 - x'_1)} \\ &\approx \text{sinc}\left(\frac{kL_1}{\pi D}(x'_2 - x'_1)\right) \end{aligned} \quad (5)$$

where $\text{sinc}(x) \triangleq \frac{\sin(\pi x)}{\pi x}$. We therefore term this the number of degrees of freedom, $DoF = \frac{2L_1L_2}{\lambda D} + 1$, and note that increasing the number of array elements beyond DoF does not improve the ambiguity function for locating a point scatterer in the scene, and only leads to an increase in the effective SNR.

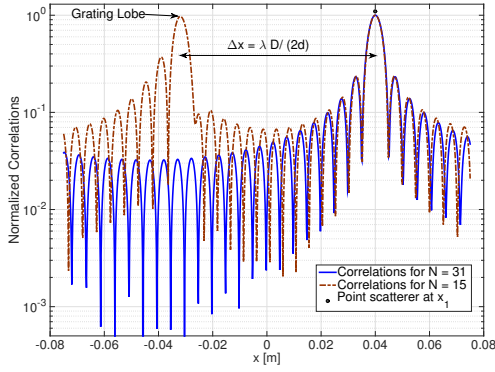


Fig. 2. Grating lobe artifact for sparse monostatic array

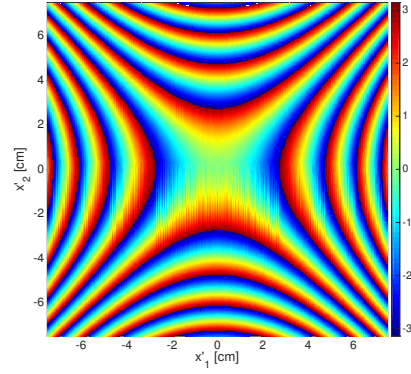
III. SPATIAL AGGREGATION AND THE PATCH PRIMITIVE

We now introduce *spatial aggregation* as a technique for constructing new dictionaries for reconstruction. The idea is to replace the point scatterer as the basic primitive for explaining the scene, with a (continuous) collection of point scatterers, adjacent to one another and having roughly constant reflection coefficient. Such a “patch” primitive is a natural model for explaining extended objects with bounded variation in the reflectivity function $\Gamma(x')$ across space; that is, for scenes where the reflectivity is a *spatially lowpass* function.

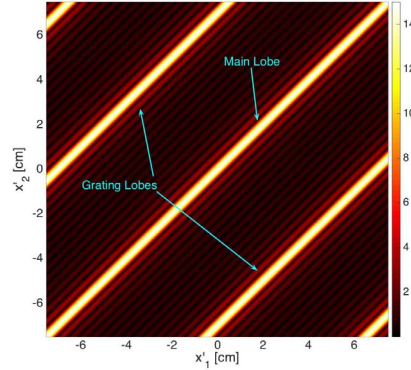
Let us consider two collection of point scatterers Ψ_1 and Ψ_2 , with their corresponding responses denoted by \tilde{r}_1 and \tilde{r}_2 , respectively. The correlation between the two responses is calculated as follows:

$$\begin{aligned}
 \tilde{r}_1^H \tilde{r}_2 &= \\
 &\sum_{n=1}^N \int_{x'_1 \in \Psi_1} \Gamma^*(x'_1) e^{j2kR(x'_1, x_n)} dx'_1 \int_{x'_2 \in \Psi_2} \Gamma(x'_2) e^{-j2kR(x'_2, x_n)} dx'_2 \\
 &\approx \iint_{\substack{x'_1 \in \Psi_1 \\ x'_2 \in \Psi_2}} \Gamma^*(x'_1) \Gamma(x'_2) e^{j\frac{k}{D}(x'_1 - x'_2)^2} \sum_{n=1}^N e^{j\frac{2k}{D}(x'_2 - x'_1)x_n} dx'_1 dx'_2 \\
 &= c_2 \iint_{\substack{x'_1 \in \Psi_1 \\ x'_2 \in \Psi_2}} \Gamma^*(x'_1) \Gamma(x'_2) H(x'_1, x'_2) \text{Dir}(\rho) dx'_1 dx'_2, \quad (6)
 \end{aligned}$$

where $H(x'_1, x'_2) \triangleq e^{j\frac{k}{D}(x'_1 - x'_2)^2}$ is the Spatial Aggregation (SA) kernel. The magnitude of the SA kernel is constant, and the phase is a non-linear function of x'_1 and x'_2 . It is easy to see that, since the SA kernel is not a function of N , the normalized correlation for the response of Ψ_1 and Ψ_2 is also independent of N for $N \gg \text{DoF} = \frac{2L_1 L_2}{\lambda D} + 1$. Figure 3 shows the phase of SA kernel and the magnitude of the Dirichlet kernel for $x'_1, x'_2 \in [-7.5, 7.5]$ cm. The key observation is that the phase of SA kernel is nearly constant across the main lobe, while exhibiting rapid variations across the grating lobes. This incoherency induced by the SA kernel is what leads to significant suppression of grating lobes.



(a)



(b)

Fig. 3. (a) Phase of SA kernel, (b) Magnitude of Dirichlet ($N = 15$)

In order to illustrate the effect of spatial aggregation, consider a simple dictionary of fixed size intervals, defined by $\mathcal{P}_w \triangleq \{\Psi = [\alpha - w/2, \alpha + w/2] : \alpha \in [-L_2/2, L_2/2]\}$. We term this a dictionary of *patches* of w cm width. For the special case of $w \rightarrow 0$, we obtain the dictionary of point scatterers. Figure 4 shows the magnitude of normalized correlations for $\Psi_1 = [3.5, 4.5]$ cm fixed, and $\Psi_2 \in \mathcal{P}_1$ for $N = 15$. We also plot the correlations of the dictionary of point scatterers for comparison. We see that the effect of SA is three-fold: (1) suppressing the grating lobe, (2) reducing the side lobe level (hence increasing the dynamic range of the image), and (3) widening the main lobe. It is important to note that the main lobe of patch correlations is representing an extended object, therefore, its width should be analyzed with respect to the width of the patch itself. In our specific example, we see that -3 dB width of the main lobe is approximately equal to the size of the patch.

IV. ESTIMATION-THEORETIC DICTIONARY TUNING

We wish to construct a dictionary that is well-matched to simple distributed targets, while providing robustness against array sparsity. Ideally, we would like to identify the smallest patch size (in order to get the best possible resolution), that provides adequate grating lobe suppression. To this end, we

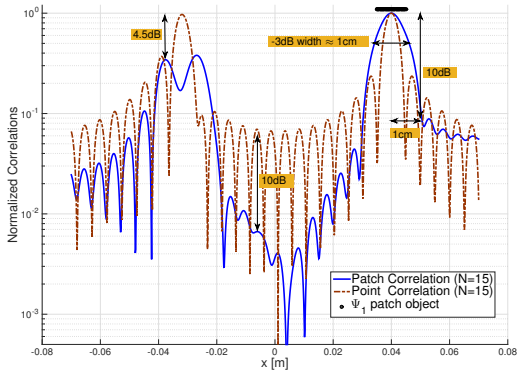


Fig. 4. Reduction of grating/side lobes by spatial aggregation

turn to the Ziv-Zakai bound (ZZB) for estimating the location of a single atom in the presence of Additive White Gaussian Noise (AWGN). The ZZB is a “global” (Bayesian) bound, i.e., it assumes a prior distribution for the unknown parameter, and bounds the mean squared error (MSE) of *any* estimator [11]. It is well-known that ZZB serves as an accurate predictor of best possible estimation performance over a wide range of SNR values. Roughly speaking, ZZB accounts for both coarse-grained errors in which the parameter estimate falls into the “wrong bin” (in our case, this is determined by grating lobes and side lobes), as well as fine-grained errors within the right bin (this is determined by the main lobe).

As the SNR increases, a point is reached where (on a log-log scale), the ZZB decreases linearly with SNR. After this point, the maximum likelihood estimate of the parameter, with high probability, is close to the true parameter value [11] (i.e., it is in the “right bin”). This threshold SNR, termed the ZZB threshold, indicates a region of operation known as the “asymptotic” regime, where the estimation performance is only limited by main lobe ambiguity (i.e., neither noise nor grating lobes can cause large estimation errors). In this regime, the ZZB is close to the Cramér-Rao Bound (CRB), which operates under the assumption that we are in the right bin. For a sparse array, our goal is to tune our dictionary parameters (i.e., the patch size) so that the ZZB threshold does not exhibit significant deterioration relative to a system with as many array elements as the DoF .

Figure 5 plots the ZZB for estimating the location of a point scatterer for different values of N , the number of array elements. We see that the bounds are indistinguishable for $N = 30$ and $N = 60$. This is a consequence of our previous observation that the normalized correlation function does not change much when we increase N beyond $DoF = \frac{2L_1L_2}{\lambda D} + 1 = 31$ elements (see Section II). On the other hand, decreasing the number of elements to $N = 15$ introduces grating lobes. The existence of the grating lobe is reflected in the corresponding ZZB curve where the threshold SNR has increased by about 13 dB compared to the dense arrays ($N = 30$ and 60). The intuition behind this is that the

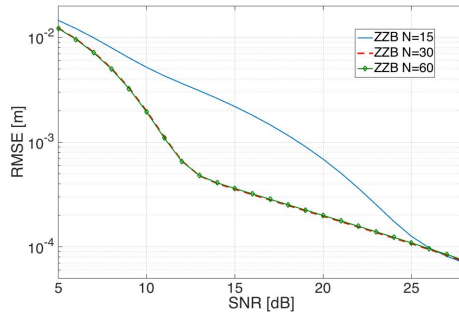


Fig. 5. ZZB for the dictionary of point-scatterers

multi-modal structure of the correlation function leads to a fundamental ambiguity in estimating the location of a single point scatterer.

Now, consider the patch-based dictionary \mathcal{P}_w for patch width $w > 0$. Our goal is to tune the parameter w such that its corresponding dictionary of patches suppresses grating lobes sufficiently for a sparse array with a given number of elements. To this end, for each candidate w , we compute the ZZB for estimating the location of a single patch given that the size of the patch is known *a priori*. The gap between the ZZB thresholds corresponding to the sparse array and a dense array is used as an indicator to verify whether the current dictionary is robust against the sparsity of the array, or whether it leads to a multi-modal correlation structure. Figure 6 shows that setting $w = 0.5$ cm leads to a 6 dB gap between the SNR thresholds corresponding to $N = 15$ and $N = 30$, whereas setting $w = 1$ cm eliminates this gap. Thus, for this particular scene geometry, array form factor, and number of elements ($N = 15$), a patch width of 1 cm is a better choice. This approach can be generalized to 2-D arrays and more complicated parameterized dictionaries of spatially extended atoms. We now focus on 2-D cross-range imaging and demonstrate the efficacy of the proposed framework through experimental data.

V. EXPERIMENTAL SETUP

Our hardware testbed is a 60 GHz continuous-wave radar transceiver, equipped with dual high-gain horn antennas [12]. We use a mechanical platform to move the imager on a plane parallel to the scene, thereby emulating a 2D array of sensors. The travel distance of the imager is of the order of the form factor of a portable handheld device (covering a $15 \text{ cm} \times 15 \text{ cm}$ area). We consider two uniform planar array configurations: (1) dense array of 30×30 elements (i.e. $d = \lambda = 0.5 \text{ cm}$), (2) sparse array of 15×15 elements (i.e. $d = 2\lambda = 1 \text{ cm}$). At each step of movement, the scene response is measured and stored in a vector. We consider a scene of copper strips that is placed parallel to the array at a distance $D = 30 \text{ cm}$ (Figure 7).

The first reconstruction method that we consider is standard SAR processing, which may be viewed as matched filtering (MF) with respect to a point scatterer based signal model [13].

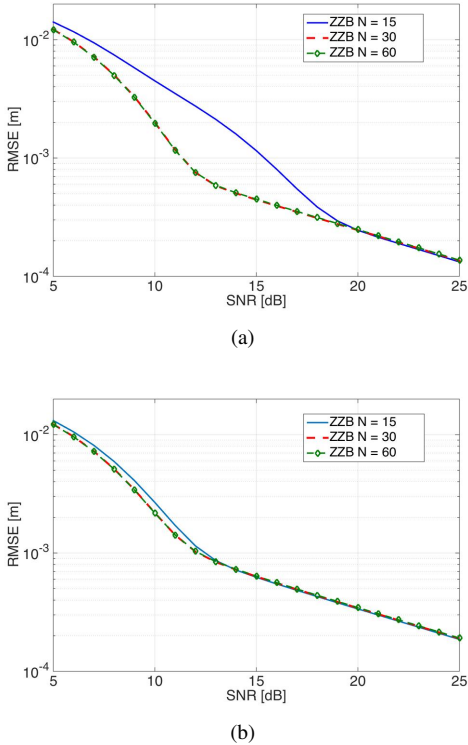


Fig. 6. ZZB for estimating the location of a single patch in the dictionary of (a) patches of size $w = 0.5$ cm (b) patches of size $w = 1$ cm.

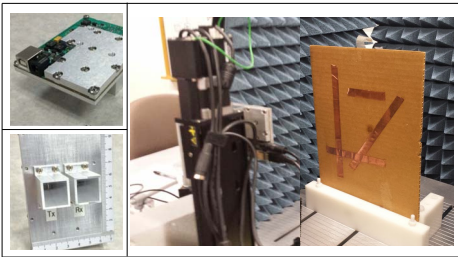


Fig. 7. Experimental data collection using 60 GHz radar system.

The second approach is based on computing the correlation of the measured response with the responses of $1\text{cm} \times 1\text{cm}$ square patches; that is, the collection of patches obtained by sliding a $1\text{cm} \times 1\text{cm}$ window over the entire scene. We refer to this approach as patch-based MF.

Figure 8 (left column) show the results of point-based MF. We see that grating lobes lead to significant deterioration in image quality for the sparse array. Figure 8 (right column) shows the result of patch-based MF. We see significant improvement in the image quality, in terms of suppressing the grating lobes and increasing the dynamic range (e.g. the horizontal strip at the bottom of the scene becomes visible for the dense array deployment). In the next section, we investigate a new technique for image reconstruction that leverages the “sparse representation” of the scene in the dictionary of patches. This parsimonious signal model, with appropriately designed estimation algorithms, allows us to “super-resolve”

beyond the limits of conventional radar theory [14].

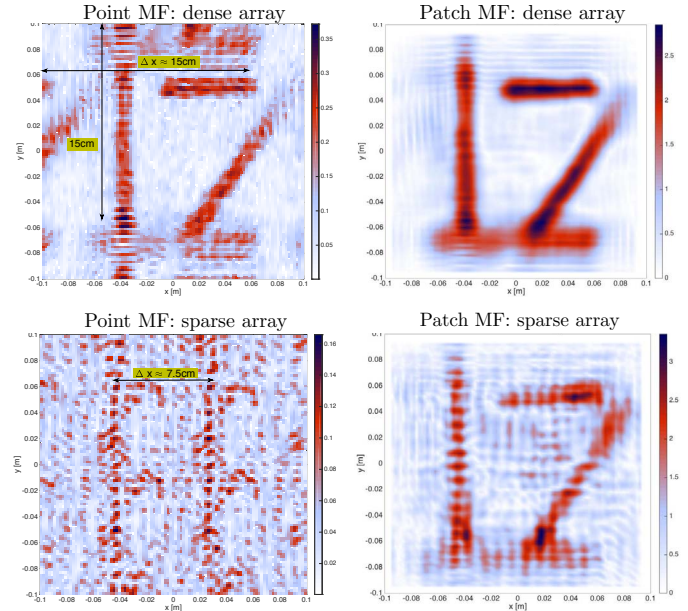


Fig. 8. Point-based v.s. patch-based matched filtering

VI. SPARSE RECONSTRUCTION

We formulate image formation as sparse reconstruction [15], approximating the scene response by a linear combination of a few patch responses from our previously constructed dictionary \mathcal{D} . To this end, we use a greedy iterative algorithm named Newtonized Orthogonal Matching Pursuit (NOMP) [9], [10], which is a generalization of the well-known Orthogonal Matching Pursuit (OMP) [16] to a continuously parametrized overcomplete basis using Newton refinements. We note that in [9], [10], the NOMP algorithm has been applied to estimation of frequencies in a mixture of sinusoids, however, the algorithm is applicable for sparse approximation in any continuously parametrized overcomplete dictionary. Greedy iterative approaches (e.g., OMP and NOMP) are particularly attractive due to their low computational complexity and ease of implementation [15].

For a scene containing \mathcal{K} patches, the overall response is modeled as

$$\mathbf{y} = \sum_{i=1}^{\mathcal{K}} g_{\alpha_i} \tilde{r}_{\alpha_i} + \mathbf{z}, \quad (7)$$

where $g_{\alpha_i} \in \mathbb{C}$ denotes the complex gain for i^{th} patch, and $\mathbf{z} \sim \mathcal{CN}(0, \sigma^2 \mathbb{I}_N)$ is the AWGN. We now present a high-level description of NOMP for sparse recovery in the radar imaging problem. Let Λ be the set of detected patches. In each iteration of the algorithm, an atom that yields the greatest improvement in the approximation quality is identified and added to Λ . After that, a *cyclic refinement* step is applied to all the atoms in Λ (i.e., the atoms that have been estimated in the previous iterations), therefore giving them a chance to re-evaluate their estimates to incorporate the effect of newly

detected atom. We do not make *a priori* assumptions on the number of patches, and set the stopping criterion based on the relative energy reduction of the residual signal (i.e., the portion of the signal not explained by the currently estimated set of patches). We stop looking for further patches when the relative energy reduction of the residual goes below a threshold, denoted by ϵ . The iterative sparse reconstruction algorithm is stated as follows:

- 1) Let $\mathbf{q}_0 = \mathbf{y}$, $\varepsilon_{q_0} = \|\mathbf{q}_0\|^2$, and loop counter $i \leftarrow 1$.
- 2) Find $\lambda = \arg \max_{\beta} \left\{ \frac{|\mathbf{q}_{i-1}^H \tilde{\mathbf{r}}_{\beta}|}{\|\mathbf{q}_{i-1}\| \cdot \|\tilde{\mathbf{r}}_{\beta}\|} : \tilde{\mathbf{r}}_{\beta} \in \mathcal{D} \right\}$. Set $g_{\lambda} = \frac{(\tilde{\mathbf{r}}_{\lambda}^H \mathbf{q}_{i-1})}{\|\tilde{\mathbf{r}}_{\lambda}\|^2}$, and update $\Lambda \leftarrow \Lambda \cup \{(\lambda, g_{\lambda})\}$.
- 3) Cyclicly refine centers/gains for all the patches in Λ .
- 4) Update all gains by least squares for best approximation of \mathbf{y} with the atoms chosen so far.
- 5) Find the new residual $\mathbf{q}_i = \mathbf{y} - \sum_{\lambda \in \Lambda} g_{\lambda} \tilde{\mathbf{r}}_{\lambda}$, and compute its energy $\varepsilon_{q_i} = \|\mathbf{q}_i\|^2$.
- 6) If $|\varepsilon_{q_i} - \varepsilon_{q_{i-1}}|/\varepsilon_{q_0} > \epsilon$, then set $i \leftarrow i + 1$, and go back to Step 2, otherwise, declare Λ as the output of the program.

Figure 9 shows the result of patch detection algorithm for the same scene of copper strips, with only 15×15 equispaced emulated array elements (sparse array). The dictionary \mathcal{D} contains all the $1.5\text{cm} \times 1.5\text{cm}$ square patches. We see that the algorithm is able to detect the horizontal strip at the bottom of the scene, despite the sparsity of the array, which is a significant improvement over the MF processing results in Figure 8.

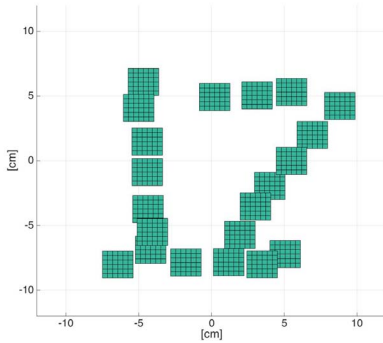


Fig. 9. Image reconstruction using NOMP algorithm in the sparse array configuration. The patch sizes are fixed ($1.5\text{cm} \times 1.5\text{cm}$), and we only refine the location of patches.

VII. GENERALIZATIONS

We now briefly discuss potential avenues for generalizing the proposed framework. In the construction of the dictionary of spatially extended atoms, we explicitly incorporate information about the array geometry in computing the response for each atom. This approach allows for the design of a dictionary that is well-matched to both the geometry of the array, and the nature of the scene being imaged, and can be easily extended to other settings, such as non-uniform arrays.

Dynamic Dictionaries: One of the problems associated with scene-based dictionary design is that the number of atoms in the dictionary may become excessively large in order to capture various shapes and sizes of the targets in the scene. This may lead to computational bottlenecks, especially for real-time applications. One approach to alleviate this problem is to construct a dynamic dictionary by bootstrapping from a base dictionary characterized with a few parameters, with a relatively small number of atoms. Additional atoms could then be added to this base dictionary during image reconstruction. For example, the dictionary of fixed-size square patches employed in Section VI can be augmented by allowing modification of patch sizes to better approximate the response to a given scene. This is easily accomplished by refining the width of patches along with their centers and gains in Step (3) of the NOMP algorithm. Figure 10 shows the output of NOMP where we start with the dictionary of $1.5\text{cm} \times 1.5\text{cm}$ patches as the base, and then refine the sizes of the detected patches throughout the reconstruction process.

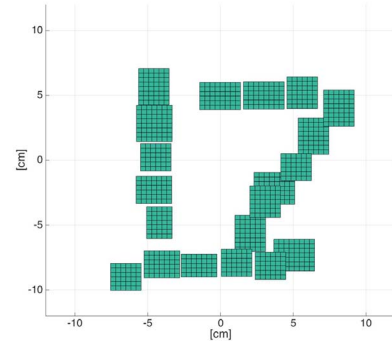


Fig. 10. Image reconstruction using NOMP algorithm in the sparse array configuration. We refine both the location and size of rectangular patches.

As another example, consider a dictionary of circular patches. Figure 11 shows the output of NOMP algorithm where we use the collection of 1cm radius atoms as the base dictionary, but then allow for both center and radius refinements. We see that the general structure of the scene is reflected in the image, including the horizontal strip at the bottom of the scene. An advantage of the circular dictionary is that the spatial size of the atoms is controlled by a single parameter (radius), hence dynamic adaptation is more computationally efficient compared to reconstruction using a dictionary of square patches.

VIII. CONCLUSIONS

We have shown that short-range radar imaging requires new models that account for scene and transceiver geometry, as well as the number of transceiver elements. For sparse arrays, the patch-based models introduced here suppress grating lobes, while being compatible with the spatially lowpass nature of typical scenes. An important topic for future work, especially for sparse arrays, is to extract and employ Doppler information as well.

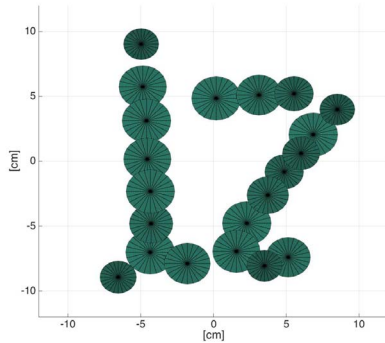


Fig. 11. Image reconstruction using NOMP algorithm in the sparse array configuration. We refine both the location and size of circular patches.

IX. ACKNOWLEDGEMENT

This work was supported in part by Systems on Nanoscale Information fabriCs (SONIC), one of the six SRC STARnet Centers, sponsored by MARCO and DARPA, and by the National Science Foundation under grant CNS-1518812. The authors gratefully acknowledge Karam Noujeim (Anritsu), who built the 60 GHz transceiver used for the experimental results reported here, and Greg Malysa for conducting the experiments.

REFERENCES

- [1] S. Ahmed, A. Schiessl, F. Gumbmann, M. Tiebout, S. Methfessel, and L. Schmidt, "Advanced microwave imaging," *Microwave Magazine, IEEE*, vol. 13, pp. 26–43, Sept 2012.
- [2] D. W. Hawkins, *Synthetic aperture imaging algorithms: with application to wide bandwidth sonar*. PhD thesis, University of Canterbury, Christchurch, New Zealand, 1996.
- [3] J. Camacho, M. Parrilla, and C. Fritsch, "Phase coherence imaging.," *IEEE transactions on ultrasonics, ferroelectrics, and frequency control*, vol. 56, no. 5, pp. 958–974, 2009.
- [4] C. Martín, O. Martínez, L. Ullate, A. Octavio, and G. Godoy, "Reduction of grating lobes in saft images," in *Ultrasonics Symposium, 2008. IUS 2008. IEEE*, pp. 721–724, IEEE, 2008.
- [5] A. Ponnle, H. Hasegawa, and H. Kanai, "Suppression of grating lobe artifacts in ultrasound images formed from diverging transmitting beams by modulation of receiving beams," *Ultrasound in medicine & biology*, vol. 39, no. 4, pp. 681–691, 2013.
- [6] E. J. Luminati, *Wide-angle multistatic synthetic aperture radar: Focused image formation and aliasing artifact mitigation*. PhD thesis, Air Force Institute of Technology, Wright-Patterson Air Force Base, Ohio, USA, 2005.
- [7] M. Cetin, I. Stojanovic, N. Onhon, K. Varshney, S. Samadi, W. Karl, and A. Willsky, "Sparsity-driven synthetic aperture radar imaging: Reconstruction, autofocusing, moving targets, and compressed sensing," *Signal Processing Magazine, IEEE*, vol. 31, pp. 27–40, July 2014.
- [8] S. Samadi, M. Cetin, and M. Masnadi-Shirazi, "Sparse representation-based synthetic aperture radar imaging," *Radar, Sonar Navigation, IET*, vol. 5, pp. 182–193, Feb 2011.
- [9] B. Mamandipoor, D. Ramasamy, and U. Madhow, "Newtonized orthogonal matching pursuit: Frequency estimation over the continuum," *CoRR*, vol. abs/1509.01942, 2015.
- [10] B. Mamandipoor, D. Ramasamy, and U. Madhow, "Frequency estimation for a mixture of sinusoids: A near-optimal sequential approach," in *3rd IEEE Global Conference on Signal and Information Processing (GlobalSIP)*, 2015.
- [11] H. Van Trees and K. Bell, *Bayesian Bounds for Parameter Estimation and Nonlinear Filtering/Tracking*. Wiley, 2007.
- [12] K. Noujeim, G. Malysa, A. Babveyh, and A. Arbabian, "A compact nonlinear-transmission-line-based mm-wave sfcw imaging radar," in *44th European Microwave Conference (EuMC)*, pp. 1766–1769, Oct 2014.
- [13] R. Bamler, "Principles of synthetic aperture radar," *Surveys in Geophysics*, vol. 21, no. 2-3, pp. 147–157, 2000.
- [14] B. Mamandipoor, G. Malysa, A. Arbabian, U. Madhow, and K. Noujeim, "60 ghz synthetic aperture radar for short-range imaging: Theory and experiments," in *48th Asilomar Conference on Signals, Systems and Computers*, pp. 553–558, Nov 2014.
- [15] J. Tropp and S. Wright, "Computational methods for sparse solution of linear inverse problems," *Proceedings of the IEEE*, vol. 98, pp. 948–958, June 2010.
- [16] J. Tropp and A. Gilbert, "Signal recovery from random measurements via orthogonal matching pursuit," *IEEE Transactions on Information Theory*, vol. 53, pp. 4655–4666, Dec 2007.